Journal of Alloys and Compounds 1004 (2024) 175851

Contents lists available at ScienceDirect

Journal of Alloys and Compounds

journal homepage: www.elsevier.com/locate/jalcom

Unraveling the mechanics of directional coarsening in single crystal Ni-based superalloys via laser peening: Insights from experimental characterization and microstructural analysis

Noah Holtham [a], Nicholas Brooks [a], Russell Rowe [a], Lloyd Hackel [b], Alireza Zargaran [c], Keivan Davami [a,*]

[a] Department of Mechanical Engineering, The University of Alabama, Tuscaloosa, AL, USA
[b] Metal Improvement Company, Curtiss Wright Surface Technologies, Livermore, CA, USA
[c] Graduate Institute of Ferrous & Eco Materials Technology (GIFT), Pohang University of Science and Technology (POSTECH), Pohang, Republic of Korea

ARTICLE INFO

Keywords:
Surface hardening
Ni-based superalloys
Laser peening
Rafting behavior
Scanning transmission electron microscopy
Energy dispersive x-ray spectroscopy

ABSTRACT

Surface treatment techniques, like laser peening, enhance the longevity of Ni-based superalloy components by reinforcing their microstructure against surface-initiated damage. Recent findings suggest that these methods may also influence precipitate coarsening behavior at high temperatures, leading to rafting phenomena. This study extensively examined γ' rafting in single crystal Ni-based superalloy CMSX-4 post laser peening and heat treatment. X-ray diffraction revealed surface compressive stresses (-400 MPa to -800 MPa), transitioning to tensile stresses at greater depths before returning to an unstressed state. Correlation with electron microscopy indicated horizontal coarsening in compressive regions and vertical coarsening in tensile regions due to misfit and residual stresses aiding diffusion. Plastic strain near the LPed surface was measurably increased with lattice misorientation values around 5° before returning to an unstrained state after heat treatment due to rafting-aided recovery and defect reorganization. Secondary γ' precipitates with a radius of approximately 10 nm occupied γ channels between rafted precipitates, indicating solute element diffusion and supersaturation. Energy dispersive x-ray spectroscopy showed a significant depletion of γ'-forming elements around rafted primary precipitates, highlighting preferential solute diffusion.

1. Introduction

The single crystal Ni-based superalloy, CMSX-4, has been a choice material for gas turbine engines for several decades due to its remarkable strength under extreme thermomechanical loading conditions. Its robustness is largely owed to the $L1_2$ intermetallic phase γ' (Ni_3Al) which accounts for ~70 % of the total material volume. The ordered nature of the γ' precipitates means that the passing of a single dislocation creates a disruption in the atomic stacking sequence as well as a chemical imbalance, known as an anti-phase boundary (APB). Therefore, a second dislocation is required to pass through the same plane and eliminate the APB, which requires significantly more energy than the passage of a single dislocation through the disordered γ phase [1]. Additionally, the lattice parameter of γ' is slightly larger than that of the surrounding γ solid solution for a negative misfit alloy like CMSX-4 [2,3]. The discrepancy is not large enough for the precipitates to lose coherency with the matrix, but it does create a compressive stress field within the γ channels which effectively reduces dislocation mobility. Further strengthening of the γ phase occurs by the addition of solid solution elements such as Cr, W, Re, and Ta which act to fortify the matrix. These strengthening mechanisms all work in concert to give CMSX-4 its remarkable properties at a wide range of stresses and temperatures. However, because the strength contribution of the γ' is very high, any change in their morphology or distribution will cause a significant change in mechanical performance. This is especially important during long-term thermomechanical exposure where the intense heat and loading can cause microstructure-level distortions [4].

One such microstructural evolution during service is known as directional coarsening or rafting. This is a common phenomenon in CMSX-4 in which the superposition of applied stress (i.e., the centripetal force on a rotating turbine blade) and precipitate misfit stresses result in the preferential coarsening of γ' along a single axis (parallel to the

* Corresponding author.
E-mail address: kdavami@eng.ua.edu (K. Davami).

https://doi.org/10.1016/j.jallcom.2024.175851
Received 5 April 2024; Received in revised form 29 July 2024; Accepted 3 August 2024
Available online 5 August 2024

direction of applied compressive stress for a negative misfit alloy like CMSX-4) [4]. During the process of rafting, the cuboidal γ' precipitates take on a rectangular morphology and coalesce into one another (Fig. 1a). The rafts form to reduce the internal energy of the system, but in doing so, reduce the interfacial surface area between the matrix and the precipitates, and consequently degrade coherency strengthening effects. Typically, rafting is seen as a detrimental effect which is indicative of a turbine blade nearing the end of its service life. Nabarro showed that rafted microstructures cause accelerated creep strain in the low-temperature, high-stress regime [5]. Additionally, the low cycle fatigue (LCF) behaviors of rafted CMSX-4 and CMSX-6 were studied by Ott and Mughrabi [6] who found that cracks only propagated through the γ and γ/γ' interfaces rather than through the γ' itself. Consequently, rafts parallel to the crack propagation direction resulted in lower LCF lives as the cracks were able to traverse the elongated interfaces with relative ease. However, results from the same work showed that rafts perpendicular to the crack propagation direction were able to block the cracks as they could not break through the precipitates, resulting in an increased LCF life.

With the knowledge that rafting may be beneficial in certain scenarios, work has been undertaken to determine whether intentionally rafting the microstructure of single crystal Ni-based superalloys before they are put into service, known as 'pre-rafting', could provide enhanced strength against creep deformation. Kamaraj tested single crystal Ni-based superalloy (SRR99) specimens under creep loading in both the pre-rafted and as-cast microstructural conditions [7]. They found that while the as-cast microstructure took longer to rupture in most stress/temperature combinations, the pre-rafted condition produced equivalent or greater rupture times at 1050 ℃ and stresses below 150 MPa. The reasoning given for these results is that under high stress, dislocation cutting is the predominant deformation mechanism in which rafted precipitates do not offer any additional strengthening and are likely detrimental due to the associated decrease in interfacial strengthening. However, at low stresses, dislocations do not have the energy to cut through the γ' precipitates and can only propagate by looping [8]. It follows that if the precipitates are coarsened in a specific direction such that the dislocations must bypass the long edge, more energy would be required to do so, and thus creep strength would be improved. Coakley et al. studied this hypothesis by testing the creep strength of pre-rafted CMSX-4 under a constant stress of 825 MPa at various temperatures [2]. The pre-rafted specimens showed substantially greater resistance to creep-induced strain than the as-cast microstructure during the test at 650 ℃ but at temperatures above 715 ℃, the creep rate for the rafted microstructure increased dramatically. It was found that the increased creep life of the pre-rafted specimen is attributed to preexisting dislocations in the rafted microstructure which hindered the generation and slip of further dislocations, though this was only true for the low-temperature/high-stress case (715 °C/825 MPa). In the high-temperature/low-stress case (1150 °C/100 MPa), the rafts degraded creep strength. While there is debate in the literature regarding the benefit of pre-rafting, many of these previous studies have evaluated the effects of rafting throughout the bulk material without considering localized rafting. By its very nature, rafting only enhances strength directionally and when treating a component with a complex geometry (like a turbine blade), some of the stress components may be misaligned with the rafts which can cause weakening and premature failure.

Given the prevalence of rafting in single crystal Ni-based superalloys, many studies have sought to understand whether manufacturing processes themselves can alter coarsening characteristics, even in the absence of externally applied stresses. This is especially important given that the metallurgical development of traditionally manufactured Ni-based superalloys has effectively reached maturity, and further increments of mechanical enhancement must come in the form of post-processing techniques such as shot peening (SP), deep cold rolling (DCR), or laser peening (LP) which can further strengthen the surface of turbine blades in a localized manner. In a recently published study by Tang et al., it was determined that rafting can occur through a combination of LP and heat treatment [9] via a combination of residual stresses and enhanced diffusion kinetics from the high-temperature exposure, though no specific microstructural mechanism was proposed. Similar results were found by Biermann et al. where rafting occurred following SP and annealing [10]. Interestingly, the rafts always formed along (100) crystallographic planes that were closest to parallel with the treated surface, indicating their preference for specific planar growth. Moreover, Bogachev et al. showed the relationship between cold work intensity and raft formation following SP and thermal exposure at 1100 °C [11]. Also shown in this work was the presence of recrystallized (RXed) grains following thermal exposure, which can be problematic since creating grain boundaries in an otherwise single crystal introduces initiation sites for hot corrosion [12]. For this reason, there is significant interest in utilizing an alternative peening method, LP, which is far less likely to induce RX while still greatly improving surface strength against surface-initiated failure mechanisms [13,14], to treat CMSX-4. While these studies tend to agree that some surface engineering processes can contribute to directional coarsening, none have studied how the rafting thermodynamics are altered due to LP, a technique that creates markedly less plastic deformation than its peers for

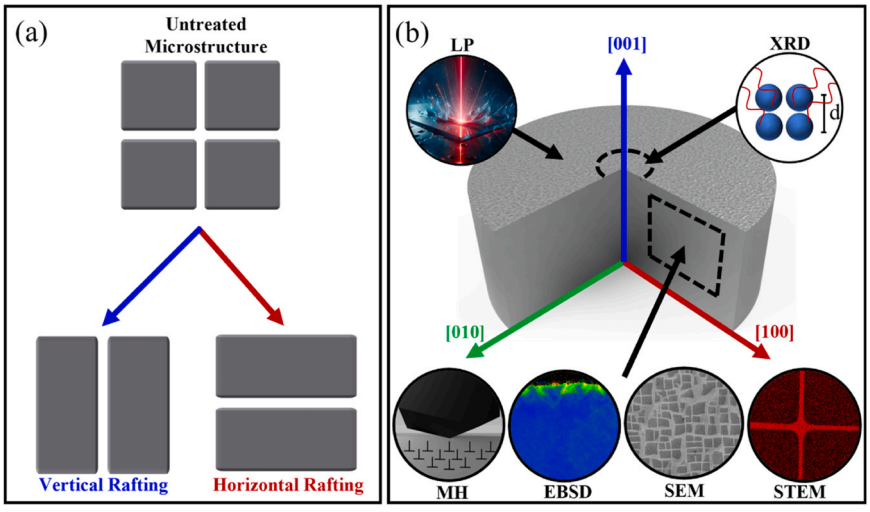

Fig. 1. Schematic illustrations showing the (a) transition from a cuboidal γ/γ' microstructure to either a horizontal or vertically rafted morphology and (b) the planes and directions in which treatment and testing procedures were performed.

comparable gains in surface strength [15,16].

In this work, the precipitate coarsening behavior of CMSX-4 under 1100 °C exposure following LP was scrutinized and corresponding morphological, chemical, and mechanical properties were detailed. The findings of this study contribute to the growing body of research on the effects of LP on single-crystal Ni-based superalloys and their corresponding directional coarsening behavior.

2. Experimental methods

2.1. Specimen preparation

The material utilized in this study is single crystal Ni-based superalloy CMSX-4 with the composition listed in Table 1. The specimens were cast as cylindrical rods having a length of 130 mm and a diameter of 23 mm with the length of the bar oriented along the [001] crystallographic direction. The cylindrical bar was then sectioned into 10 mm disks via wire electric discharge machining (wire-EDM) and LPed on the flat face normal to the [001] crystal/growth direction (Fig. 1b). Specimens were then heat treated at 1100 ℃ for 1 hr to alleviate deleterious residual stresses left over from machining.

2.2. Laser peening

All LP treatments for this work were performed by Curtiss-Wright Surface Technologies (Livermore, USA) using an industrial-grade Q-switched, Nd:YLF Nd-Glass master oscillator power amplifier laser operating at 16 J/pulse with a pulse duration of 18 ns and a 1053 μm wavelength in the water-confined mode with no ablative coating. LP was conducted on the circular cross section of the CMSX-4 discs over a 415 mm^2 area. Here, the layer of deionized water (approximately 1 mm thick) acted as a tamping medium to confine the plasma volume. An ablative media was not utilized to mimic LP treatments performed on an industrial scale. An amorphic lens was used to shape the rectangular laser beam into a square cross section with a uniform energy profile [18]. The final spot size of the laser beam was varied depending on the laser power density required. Square laser spots on individual layers were overlapped by 3 % while subsequent layers were offset by 33 % in the X and Y dimensions to achieve 100 % coverage over 3 layers as is shown in Figure A.1. While several processing parameters play a role in the effectiveness of LP, final spot size and laser power density are the most important as they are directly related to the magnitude of the pressure wave generated by the plasma, which in turn controls the magnitude of plastic deformation and compressive residual stresses [13]. It has been experimentally determined that plastic deformation will occur from LP when the magnitude of the induced pressure wave exceeds the material's Hugoniot Elastic Limit (HEL), which is a function of Poisson's ratio (ν) and dynamic yield stress (σ_{dyn}, or ~1.2 times the static yield strength), and achieves peak deformation values between 2 and 2.5 times the HEL [19].

$$HEL = \frac{1-\nu}{1-2\nu}\sigma_{dyn} \tag{1}$$

It then follows that utilizing a large spot size coupled with increasing the laser power density beyond 1·HEL and up to 2.5·HEL yields successively deeper residual stresses and work hardening effects. Consequently, there will be significantly different microstructural gradients between specimens treated with different power densities. For this reason, spot sizes ranging from 2.98 mm – 4.71 mm and power densities ranging between 4 GW/cm^2, 7 GW/cm^2, and 10 GW/cm^2 were chosen to generate pressure pulses of approximately 1·HEL, 2·HEL, and 2.5·HEL in magnitude respectively utilizing Eqs. 2–4:

$$I_0 = \frac{4E}{\tau\pi d^2} \tag{2}$$

$$Z = \frac{2}{\frac{1}{Z_1}+\frac{1}{Z_2}} \tag{3}$$

$$P = 0.01\sqrt{\frac{\alpha}{2\alpha+3}}\sqrt{Z}\sqrt{I_0} \tag{4}$$

where I_0 (GW/cm^2) is the laser power density which is obtained by dividing the laser energy E (J) by the pulse duration τ (ns) and the area of the spot (cm^2). The total shock impedance Z (g/cm^2·s) of the target material and the ablative material are Z_1 and Z_2, respectively, and the constant α is the efficiency of the plasma-materials interaction (typically $\alpha = 0.2$ for water confinement [20]). However, since LP was carried out without the ablative material in this study, only the shock impedance of the target material (CMSX-4) and the confining water media were considered in calculations ($Z_{H2O} = 1.65 \times 10^5$ g/cm^2s, $Z_{CMSX\text{-}4} = 4.14 \times 10^6$ g/cm^2s) [13,21]. Lastly, the depth of plastic deformation (L_p) induced by LP can be numerically approximated by Eq.5:

$$L_p = \frac{C_{el}C_{pl}\tau}{C_{pl}-C_{el}}\left(\frac{P+HEL}{2HEL}\right) \tag{5}$$

where C_{el} is the elastic wave velocity, C_{pl} is the plastic wave velocity, and τ is the pulse width. Eq. 5 predicts the depths of plastic deformation for LP4, LP7, and LP10 to be 1.1 mm, 1.3 mm, 1.4 mm for a single layer of peening respectively. However in this case, 3 layers of LP were conducted on each specimen which causes residual stresses to be driven deeper than what is predicted by Eq. 5 [22,23].

While optimizing the laser power density can yield the highest degree of residual stresses and work hardening, the depth of these beneficial effects may be quite shallow after a single shot depending on the material chosen. For this reason, three layers of peening in the same location were applied successively to drive the residual stresses deeper into the material [19,24]. Specimens were then exposed to 1100 °C in air for 100 hours to understand their rafting behavior. This temperature was specifically chosen to hasten the kinetics of rafting and for direct comparison with the results reported by Bogachev et al. [11]. All specimen treatment parameters can be found in Table 2.

Prior to optical and electron microscopy analysis, specimens were

Table 2
Specimen identification details.

Specimen ID	Laser Power Density	Spot Size	Peak Pressure	Layers of LP	Heat Treatment
Untreated	-	-	-	-	-
LP4	4 GW/cm^2	4.71 mm	3.66 MPa	3	-
LP4 + HT	4 GW/cm^2	4.71 mm	3.66 MPa	3	1100 ℃, 100 hr
LP7	7 GW/cm^2	3.56 mm	4.84 MPa	3	-
LP7 + HT	7 GW/cm^2	3.56 mm	4.84 MPa	3	1100 ℃, 100 hr
LP10	10 GW/cm^2	2.98 mm	5.78 MPa	3	-
LP10 + HT	10 GW/cm^2	2.98 mm	5.78 MPa	3	1100 ℃, 100 hr

Table 1
Chemical composition in wt% for CMSX-4 [17].

Alloy	Cr	Co	Mo	Re	W	Al	Ti	Ta	Hf	Ni	Density (g/cm^3)
CMSX−4	6.5	9	0.6	3	6	5.6	1	6.5	0.1	Bal	8.7

ground with SiC papers (600 – 1200 grit) and then polished using water-based diamond suspensions (9 μm – 0.05 μm) to remove imperfections and create a flat surface for observation. Short grinding times (< 5 min) and long polishing times (15 min) were used to minimize the effects of plastic deformation from specimen preparation. Specimens were then etched with aqua regia (1:3 ratio by volume of HNO_3 to HCl) for ~30 seconds to reveal the underlying microstructure.

2.3. Electron microscopy

Scanning electron microscopy (SEM, *Thermo Scientific Apreo FE-SEM*) images were taken with an accelerating voltage of 20 keV in secondary electron (SE) mode. All images were taken in the same orientation with the LPed face always nearest the top of the image for consistency. Electron backscatter diffraction (EBSD, EDAX Digiview) scans were taken over a 300 μm × 300 μm area with a 0.07 μm/pixel step size to optimize resolution and scan speed. Pixels with a confidence index lower than 20 % were removed from the data set and are represented as black pixels. The hexagonal pixels were grouped into 3×3 kernels and compared with their second nearest neighbor to create kernel average misorientation (KAM) maps. Values of misorientation greater than 5° were removed from calculations to reduce the influence of pores. The magnitude and depth of the average misorientation between kernels was used to estimate the magnitude and depth of cold work for comparison between specimens.

Transmission electron microscopy (TEM) was conducted using a JEOL JEM-2100 F field emission electron microscope with STEM capabilities. Centered bright-field images were taken around the [001] crystallographic pole unless otherwise specified. Lamellas for TEM observations of approximately 10 μm in length and 5 μm in height were thinned at 5 keV until sufficiently electron transparent using a focused ion beam (FIB, TESCAN LYRA FIB-FESEM).

2.4. X-ray diffraction stress analysis

Since the stresses within single crystals are difficult to characterize using the $\sin^2\Psi$ technique, which is typical for polycrystalline materials, an alternative approach has been employed in which d-spacing is used to calculate the in-plane equibiaxial stress state from x-ray diffraction (XRD) peak profiles. In CMSX-4 and similar Ni-based superalloys, the γ and γ' phases have close lattice parameters that can cause peak overlapping for misfit values of ± 0.1–0.3 % [3]. In previous studies, a peak deconvolution method has been used to separate the γ and γ' peaks from the XRD patterns of CMSX-4 to accurately determine the lattice parameters of the two individual phases [25,26]. However, due to the poor resolution of standard laboratory x-ray diffractometers the γ and γ' peaks are difficult to resolve. Additionally, in this study the primary goal is not to accurately determine the lattice parameters of the two phases, but rather to compare the stress state imparted by LP at several power densities and correlate the stress direction with the precipitate growth direction. As such, the peaks obtained from the XRD patterns here have been left in their superimposed state, and d-spacing measurements have been made by fitting a gaussian curve to the data.

X-ray diffraction (XRD) scans were performed using an x-ray diffractometer (Bruker D8 Discover) with a Co-Kα source (40 kV, 35 mA) at a scan speed of 5.6°/min within a scanning range of $28^\circ < 2\theta < 84^\circ$ to capture the overlapped (200) γ/γ' peak around a Bragg angle of ~60° [27]. An electrolytic polisher (Proto 88–8-V3) with a saline electrolytic solution operating at a voltage of 60 kV was used to remove material from the surface of the LPed specimens up to depths of 2000–3000 μm from the treated surfaces (Figure S.1). While it is recognized that this technique may affect the residual stress state of the specimens, this specific chemical technique was selected over mechanical cutting techniques because it introduces the least amount of external stresses. Depth measurements following electro-polishing were obtained using a profilometer (KLA Tencor D-500). Initial measurements were taken ~50 μm below the surface as the recast layer from processing had to be removed (Figure S.2). XRD peaks obtained from various depths were then characterized with a Gaussian fit using Origin software's peak fitting module. The Bragg angle of the γ/γ' peaks was then used to calculate the d-spacing (d_{hkl}) using Bragg's law (Eq. 6)

$$d_{hkl} = \frac{n\lambda}{2\sin\theta} \tag{6}$$

where n is the order of diffraction (n = 1), λ is the wavelength of the Co-Kα source (λ = 0.17902 nm), and θ is half of the Bragg angle (2θ) in degrees. This calculation was performed for all γ/γ' peaks from all of the LPed specimens and the unpeened specimen. A simple, but reasonably effective residual stress calculation was then performed using Eq. 7 from Cullity [28,29] to calculate the residual stresses with depth from the LPed surfaces of the specimens. This equation can be employed given the underlying assumption that the LP-induced stresses maintain an equi-biaxial stress state on the plane perpendicular to the peening direction [30,31], or the (001) plane in this case.

$$\sigma_{hkl} = -\frac{E_{hkl}}{\nu_{hkl}}\left(\frac{d^1_{hkl} - d^0_{hkl}}{d^0_{hkl}}\right) \tag{7}$$

The elastic modulus (E_{hkl}) and the Poisson's ratio (ν_{hkl}) in the [002] direction were taken as 125 GPa and 0.39, respectively [32]. The residual stress (σ_{hkl}) is then calculated using the un-stressed d-spacing (d^0_{hkl}), obtained by etching away the machined surface of the unpeened specimen and the stressed d-spacings (d^1_{hkl}), obtained from the LPed specimens at various depths from the treated surfaces. Using Eqs. 6 and 7 above, the authors have obtained residual stress versus depth profiles from the LPed surfaces of the CMSX-4 specimens.

2.5. Rafting parameter

The rafting parameter, R, is calculated by the relation R = L/2 T where L is the length, or horizontal dimension of the γ' precipitate (parallel to the plane of material that was LPed) and T is the 'thickness', or vertical dimension of the γ' precipitate. Measurements were performed using the ImageJ software package. By the nature of the rafting parameter relationship defined above, values of 'R' larger than 0.5 will naturally have a larger standard error.

2.6. Hardness testing

Microhardness testing was conducted using a microindenter (Clemex MMT-X7B) equipped with a Vickers tip operating at a peak load of ~5 N and a 13 s dwell time. The indentation matrix for all specimens was 30 × 6 with a 100 μm spacing between the indent centers in both the X and Y directions for a total sampling area of ~1.8 mm^2. This procedure follows ASTM E384–17 standard [33] which prescribes an indent spacing of at least 1.5 times the Vickers diagonal. All indents were made on the specimen face parallel to the (010) plane which is perpendicular to the treated face to allow for the collection of microhardness data with depth from the treated surface. Baseline microhardness measurements were obtained from the same plane to account for the anisotropic material properties of CMSX-4 and to maintain consistency (Figure S3).

3. Results and discussions

3.1. LP-induced rafting behavior

To begin the investigation, SEM images were taken of the microstructure at several depths (0 μm – 5000 μm) from the LPed surface following heat treatment (Fig. 2). Starting from the surface, a discontinuous layer of porous resolidified material (~10 μm thick) is observable as a byproduct of the direct LP process (Figure S.2). In this case, no sacrificial ablative media was used and thus, the thin layer of material

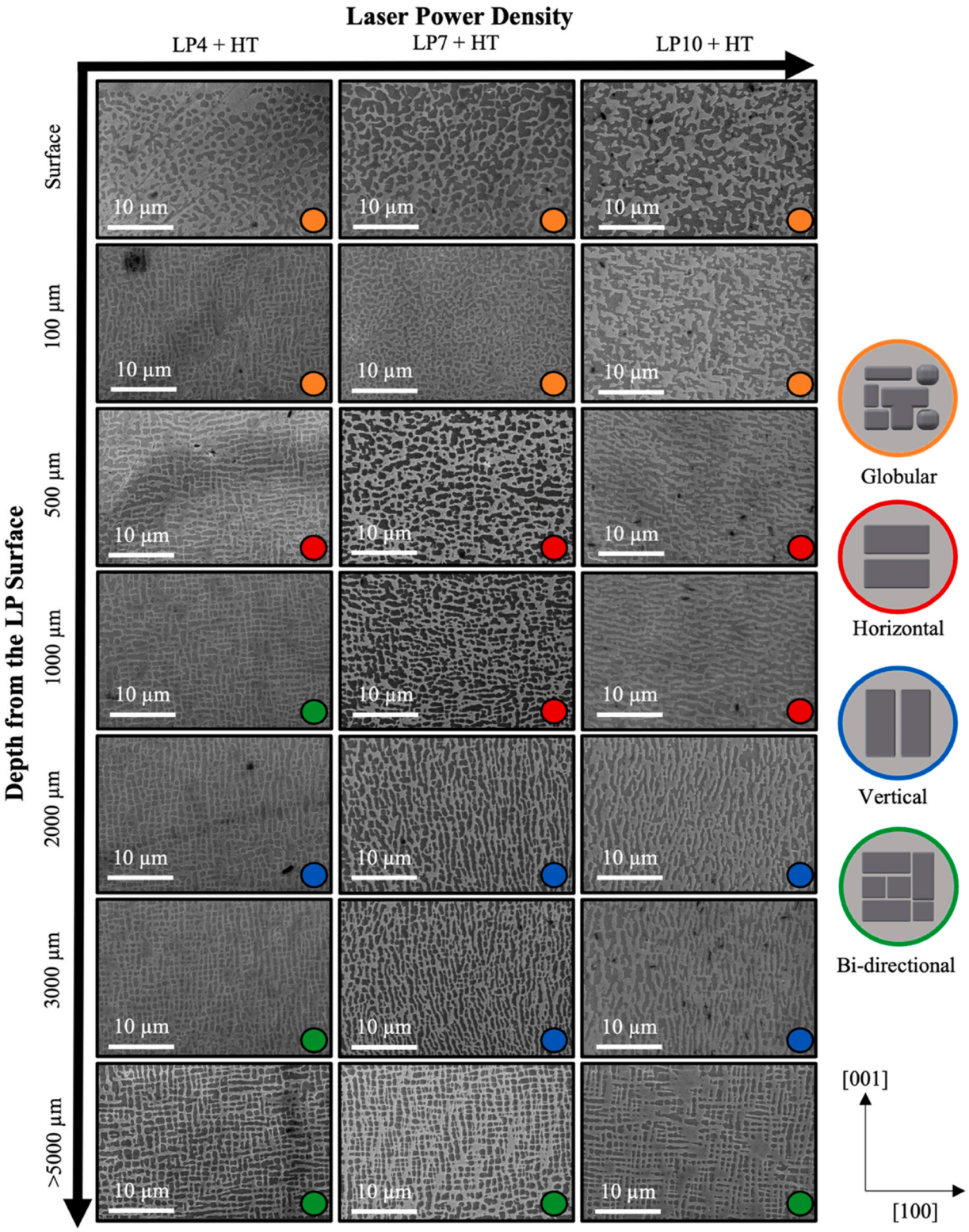

Fig. 2. SEM images of the CMSX-4 microstructure following LP at different laser power densities and subsequent heat treatment. Images were taken of the cross-sectional surface at several depths from the treated surface to show the localized nature of rafting following LP. All images were taken at the same magnification and are color-coded with a marker in their respective bottom left corners. The colors are based on the rafting parameter 'R'.

which was rapidly heated and partially ablated upon contact with the laser pulse was redeposited on the surface upon cooling. Moving just below the recast layer, one can observe γ' precipitates which have transformed from their cuboidal shape to a much more globular morphology in both the LP4+HT and LP7+HT specimens. This transformation reduces the internal energy of the system, which was significantly increased following the plastic deformation imparted via LP. While at the surface of the LP10+HT specimen, this effect is magnified as the γ' particles grew into one another such that the microstructure began to exhibit a phenomenon known as topological

phase inversion (TPI). TPI is discussed thoroughly in the literature as an evolution that occurs under extreme thermomechanical loads where the γ' phases grow into one another, isolating the γ phase into islands [34] and giving the appearance that γ' is the new matrix phase with a dispersion of γ. The rapid growth of γ' at the surface of all specimens suggests that the dislocations generated by LP accelerate coarsening significantly, potentially to a detrimental degree in the LP10+HT specimen.

Moving deeper into the material, the first evidence of rafting rather than non-directional coarsening is observed at a depth of ~500 μm in all specimens. At this depth, the intensity of cold work is reduced, and thus residual stresses have more influence on coarsening properties with a reduced contribution of dislocation-aided interface growth. Indeed, the directionality assumed by the rafts has been shown to strongly correlate with the direction of stresses [7,35] with compressive stresses causing rafting parallel to the principal stress axis and tensile stresses causing perpendicular rafting (Fig. 1a) in a negative misfit alloy such as CMSX-4 [7]. LP-induced residual stress gradients typically follow the pattern of compressive stresses near the surface and tensile stresses at greater depths with a return to the unstressed state at distances beyond the plastic penetration depth of LP [36,37], and should therefore yield rafting behavior that varies with depth from the treated surface. This can be seen in Fig. 2 as the rafting direction transitions from horizontal to vertical with increasing depth before returning to a bi-directional coarsened state (green markers). Although this general behavior is uniform across each specimen, there is also evidence of a strong dependence on the laser power density and corresponding pressure wave intensity. For example, the LP4+HT specimen transitions to a state of bi-directional coarsening at a much shallower depth than the other specimens at approximately 1000 μm. This mixed coarsening regime can be explained by the minimization of interfacial energies [38] inherent to the alloy rather than any LP-induced effects as the residual stresses have attenuated to the baseline value at these depths. The LP7+HT and LP10+HT specimens on the other hand continue horizontal rafting to a depth of 1000 μm before transitioning to vertical rafts around 2000 μm. Finally, at depths far beyond the influence of the LP process, both LP7+HT and LP10+HT presented mixed coarsening just as the LP4+HT specimen did.

These observations are qualitative of course and thus for a more quantitative approach to the SEM data, the rafting parameter 'R' was calculated using the method outlined in [39] and detailed in Section 2. It should be noted that finding the rafting parameter for a given condition is challenging as there is significant variation in raft morphology even within an isolated SEM image. This may relate to the internal microstresses as was pointed out by Biermann et al. [10], which may raise or lower the energy barrier for diffusion at a given γ/γ' interface. Fig. 3 shows the plotted results of the rafting parameter calculations. Immediately noticeable is the increasing depth at which peak horizontal rafting occurs with successively greater laser power densities. One can observe that the direction of rafting quickly moves to horizontal ($R > 0.5$) with increasing depth from the LPed surface where the coarsening is mostly uniform ($R = 0.5$). The error bars in this case represent the relative extrema of measurements of R taken from individual precipitates.

In contrast with other works which have studied the inducement of rafting via SP [10,11], this study reveals that LP creates a stress gradient that leads to horizontal rafting near the surface and vertical rafting at deeper levels with minimal levels of cold work. This controlled approach to influencing microstructural evolution offers a significant advancement over traditional methods, providing a more precise way to enhance material performance. Moreover, by using an array of laser power densities the research demonstrates a strategic method to manage rafting behavior, aligning with ongoing efforts in the literature to refine surface treatment techniques for optimizing the durability and performance of superalloys.

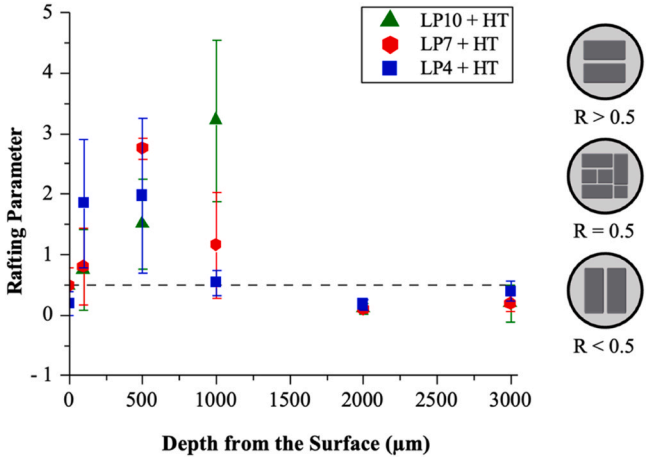

Fig. 3. Rafting parameter plotted vs. depth from the LPed surface. The non-rafted microstructure has an 'R' value of 0.5 and is marked by a dotted line. The horizontally and vertically rafted regimes have 'R' values greater and less than 0.5, respectively. Error bars represent the standard deviation and schematics illustrate the rafting directions at values of 'R' lesser, greater, or equal to 0.5.

3.2. LP-Induced material property changes and their implications

3.2.1. Residual stresses

Having shown the occurrence of rafting after LP and HT, the study will now focus on the mechanisms that control directional coarsening, beginning with residual stresses. From Fig. 4a, one can observe that the residual stress near the surface begins with a highly compressive value near the surface in each specimen before achieving maximum compressive residual stress values at ~250 – 500 μm below the surface. Although one may expect the maximum stress value to develop at the surface, this is not true for normal stresses as the elastic component is allowed to relax on a free surface and therefore the maximum stress value is measured at a small depth below [40,41]. At greater depths, the values of stress begin attenuating back to the unpeened values before transitioning to a tensile state. Moreover, a distinct shift of the Bragg peak is shown in Fig. 4b with varying depths from the LPed surface, showing the gradient of lattice strain, and consequently, the interplanar spacing (Fig. 4c). This localized residual stress/strain behavior in surface-hardened materials has been discussed many times in the literature [31,37,42,43], but what is particularly notable here is the magnitude of difference between the different laser power densities. For example, the LP10 condition clearly drives stresses deeper and more intensely than the LP7 and LP4 conditions. It is clear from this data that the numerical models developed by Peyre et al. [19], which postulate that residual stress magnitude and depth are proportional to the magnitude of the pressure wave up to a value of 2.5·HEL, are consistent with the experimental data collected here.

From the residual stress results (Fig. 4) along with the microscopy observations (Fig. 2), it can be seen that LP indeed modifies the coarsening behavior of CMSX-4, leading to the formation of γ' rafts whose orientation is, at least in part, influenced by the surrounding stress state. The superposition of the inherent coherency stresses with the LP-induced residual stresses is noteworthy here as the compressive stresses induce parallel growth, while tensile stresses induce perpendicular growth. Moreover, this correlation is more pronounced at greater depths where dislocation density is minimal. It should also be noted however that while the rafts correlate with the residual stress direction, they also have a strong crystallographic dependence. This was shown in a work by Biermann et al. where rafts grew consistently along {100} planes despite peening at several angles along a curved surface [10]. This could be attributed to the misalignment of the residual stress vectors and misfit stress vectors at oblique angles from the {100} planes

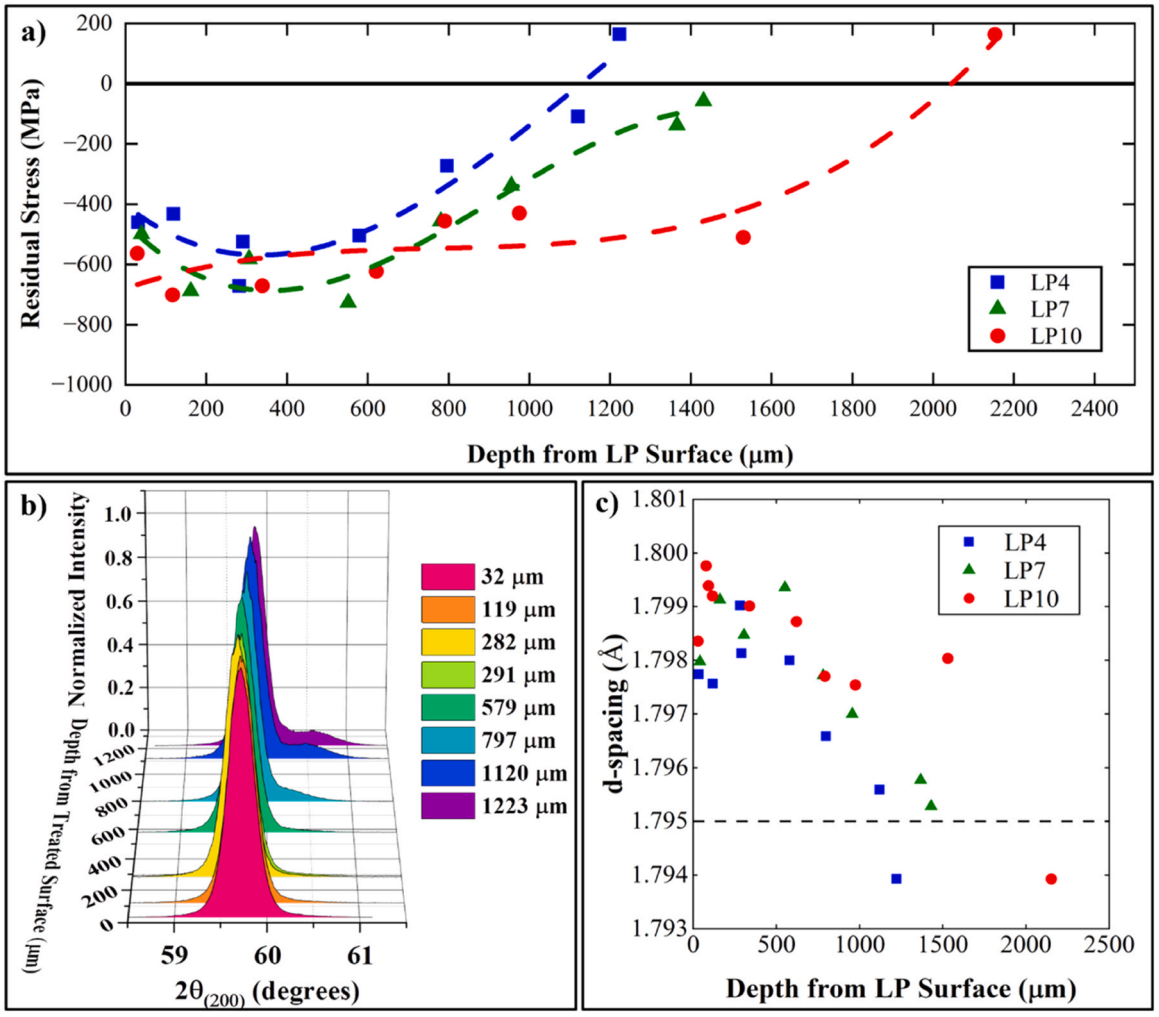

Fig. 4. Residual stress distribution in the LPed and rafted specimens. (a) The raw data points are plotted along with a third-order polynomial fitting curve to show the approximate trend of the stress profiles. (b) XRD peaks corresponding to the (200) plane plotted vs intensity at different depths from the LPed surface from LP4. (c) Interplanar spacing (d-spacing) plotted vs. depth from the treated surface for each of the LP conditions.

and thus not contributing enough driving force for directional coarsening to occur [10]. Moreover, the cube-cube interface between the ordered Ni_3Al phase and the surrounding matrix necessitates that the largest reduction in precipitate surface energy can be attained by joining two neighboring γ' faces, which lie along {100} planes [44]. Further work is required to verify the orientation dependance of the residual stress vector with raft directionality.

3.3. LP-induced microstructural changes and their implications

3.3.1. Cold work depth and lattice misorientation

Fig. 5 shows the KAM maps for the LP10 and LP10+HT specimens within a 300 μm × 300 μm area to represent the variation in cold work with increasing depth from the treated surface. From Fig. 5b, one can observe that LP generated significant plastic deformation resulting in measurable lattice rotations near the surface, as opposed to the unpeened specimen which is nearly deformation-free (Fig. 5a). It should be noted that in all LPed specimens, the depth of geometrically necessary dislocations generated by peening is markedly less than that of SPed [45,46] and DCRed [47] CMSX-4. This is largely expected as LP is known to produce relatively little cold work while achieving similar, or even superior, mechanical properties [15,37,48].

Following the heat treatment, all specimens showed evidence of dislocation relaxation as the geometrically necessary dislocations, as indicated by the KAM values, near the surface largely returned to that of the underlying material (Fig. 5c). The reorganization of dislocations generated by LP under intense thermal load is well documented [16,36] and is likely the case here. While this recovery can take many forms such as dislocation annihilation, sub-grain refinement, and RX, evidence from [49] shows that dislocations largely congregate in the interphase interface to reduce the overall misfit strain in the presence of heat. This can be seen qualitatively by correlating the KAM and SEM data where one can then make the comparison that the region in which the cold work is present, is also the region in which coarsening has the least directional dependence and produces a globular morphology (Fig. 2, orange-marked images). The high density of dislocations near the LPed surface greatly increases the free energy of the system [1], causing the coarsening thermodynamics to be driven by the reduction in lattice strain energy rather than by reducing interfacial energy. In turn, this allows coarsening to occur not only on geometric close-packed planes but also along planes that would be otherwise unfavorable for growth in the absence of high plastic deformation. Moreover, it should be emphasized that intense thermal loads did not cause RX in any of the specimens used in this work (Fig. 5c), though it may have altered oxidation performance via selective transport of Al and Cr and is a topic of future work. This is significant as the heat treatment used was identical to that used in [11] where RX clearly occurred in each SPed and DCRed specimens. Further work is required to study the nature of

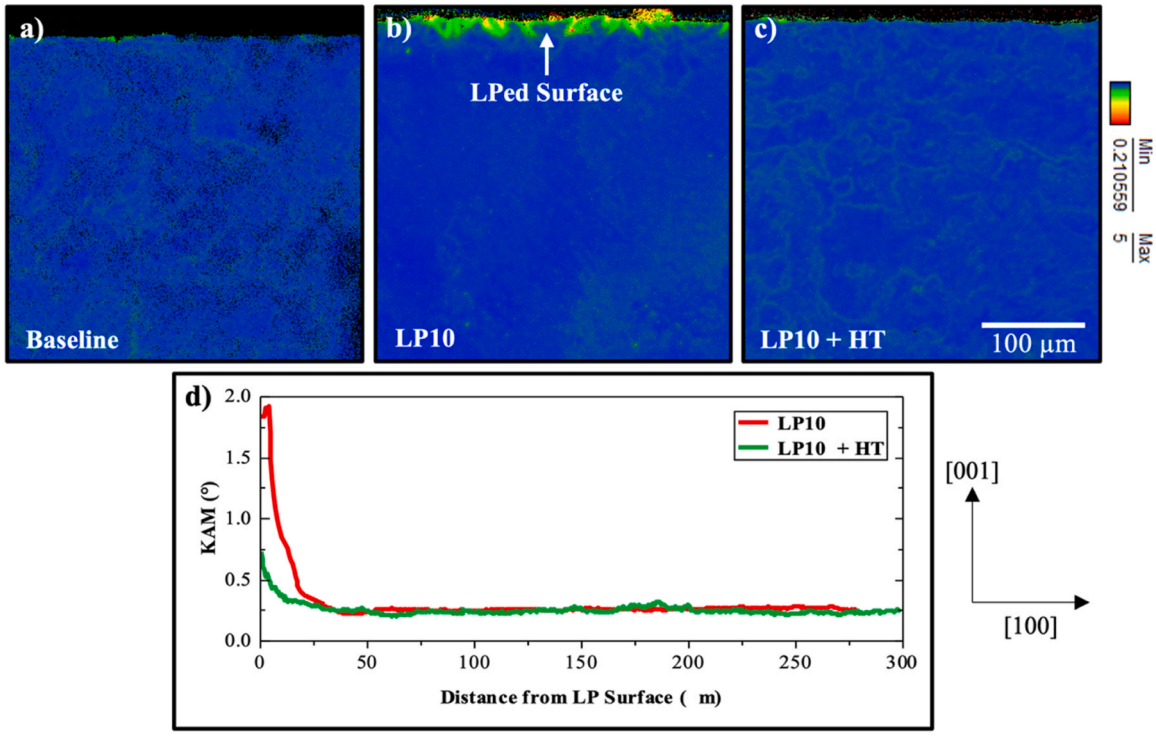

Fig. 5. Representative KAM maps of the (a) untreated, (b) LP10, and (c) LP10+HT specimen sets with the peened surface at the top of each map (if applicable). Black pixels represent the mounting material and were removed from all KAM calculations. (d) Plot of the average misorientation per unit of depth in the LP10 and LP10+HT specimen vs. depth from the treated surface shows the gradient in deformation behavior.

recovery and RX in surface-treated specimens and the effects those mechanisms have on turbine blade service lives, but these results combined with those in the literature show promise for LP as an alternative hardening technique that does not ultimately alter the single crystalline nature of the alloy.

3.3.2. *Role of LP-induced dislocations on coarsening behavior*

Beginning with the unpeened specimen, Fig. 6a shows a STEM image of a lamella extracted from an untreated specimen. Having undergone no cold work, the microstructure is nearly defect-free. The γ' precipitates present a square cross-section with ~500 nm side lengths and corners which are slightly rounded to reduce coherency strain in these concentrated areas. With this exception, the unpeened γ/ γ' interface is highly coherent. Following LP, however, the microstructure near the surface drastically changes. STEM images of lamellas taken 100 μm from the treated surface prior to thermal exposure are presented in Figs. 6b and 6c. Massive slip bands along the (111) family of planes shear through both phases with little discrimination and cause pileups at their intersections. Typically, dislocations travel preferentially through the γ channels along the {111} <110> slip system as this requires the lowest energy for movement [1]. The shearing of γ', on the other hand, is particularly unfavorable as its ordered nature requires the passing of two full dislocations (or superpartials) to remove the APB created by the first dislocation [1,50]. It is for this reason that most of the dislocations are generated in, and will travel through, the γ phase, until the point at which the dislocation pileups in the γ channels are so severe that they become energetically favorable to shear through the γ' precipitates, or if the applied stress is high enough to drive dislocations into the ordered precipitates. The plasticity behavior of CMSX-4 discussed thus far is largely reported in the literature, however, these studies are largely concerned with creep and/or fatigue loading of turbine blades in which dislocation climb and cross-slip are favorable methods of bypassing

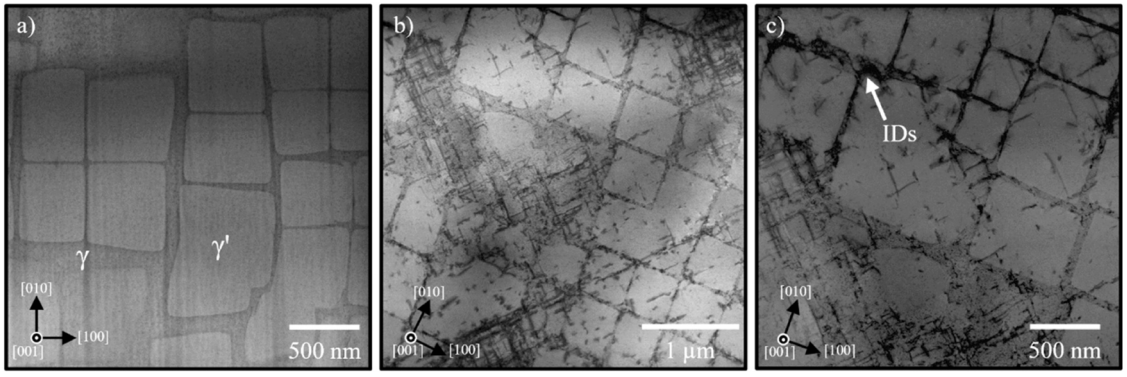

Fig. 6. STEM image of the (a) untreated specimen showing a defect-free microstructure and images of the (b, c) LP10 specimen revealing a high dislocation density within the γ channels as well as several interfacial dislocations (IDs) piled up at the γ/γ' interface. Dislocations are also seen cutting through both phases along the (111) planes.

precipitates until pileup becomes severe enough to induce shearing. In this case, LP generates a pressure wave that moves through the material at the speed of sound of that material. When this happens, dislocations must accommodate the plasticity [51] and thus precipitate shearing can occur without the prior interfacial dislocation build-up. This can be seen experimentally in Figs. 6b and 6c where dislocation density is evenly spread across the γ and γ' phases. These results are consistent with [25] where precipitate shearing was found to be the dominant plastic deformation mechanism. Additionally, the dislocations trapped at the γ/γ' interface can significantly weaken the coherency between the γ and γ' phases and aid in rafting as discussed above. Further, they have been shown to attract γ stabilizing elements, particularly Cr and Co, from the γ channels parallel to the tensile loading axis and move them to the channels perpendicular to the load axis [52]. This essentially destabilizes the γ channels in the direction of raft growth and allows the kinetics of solute transfer to accelerate.

The precise role of dislocations on the rafting behavior of single-crystal Ni-based superalloys seems to lack consensus within the scientific literature. While many reports claim that dislocations at the γ/γ' interface are necessary for relieving misfit stresses to encourage diffusion [53,54], others claim that the reduction in misfit acts to decrease the driving force for coarsening [55]. Although these arguments seem to be in opposition, one must consider that rafting is a highly directional process and that these arguments are not necessarily mutually exclusive. As stated in the previous section, the direction of elastic residual stress and strains largely governs the preferential coarsening direction [56]. If interfacial dislocations are to act in such a way that their degradation of misfit stresses reduces the elastic energy in the coarsening direction, then one can say that dislocations deter rafting. In the opposite case, where the misfit stresses are reduced in the direction perpendicular to coarsening, then dislocations can be said to have aided in rafting kinetics. Wu et al. discuss this at length in their recent work in determining the role of dislocations in rafting via phase-field modeling [57] where they show that dislocation pileups at the phase boundary significantly alter the elastic energy potential such that diffusion is promoted through the vertical channels and restricted through the horizontal channels in a loading scenario consistent with Fig. 1a for a negative misfit alloy.

3.3.3. γ' interfacial growth

In addition to aiding in solute diffusion, interfacial dislocations also play a role in the migration kinetics of the γ' phase into the surrounding matrix. As can be seen in Fig. 7b, following heat treatment, the once smooth interface between γ and γ' (Fig. 7a) now contains many grooves following rafting, which indicates the occurrence of non-uniform interfacial growth. This behavior was also supported by Link et al. who studied the coarsening behavior of γ' precipitates in CMSX-4 at 1100 °C in a dislocation-rich environment [49]. From their experiments, it was shown that small amounts of γ' dissolve at this temperature, and upon cooling with a slow rate of less than 15 °C/s, γ' re-accumulates in areas around the interfacial dislocations that are effectively pinned. This pinning mechanism occurs due to the preferential movement of dislocations to the γ/ γ' interface at high temperatures to relieve misfit strains, only to become immobilized once the misfit is reduced during cooling. Given that the cooling rate used in this work was 15 °C/s, the mechanism proposed by Link et al. is likely behind the γ' grooving here as well. Near the treated surface, the TPI zone provides insight into the coarsening behavior at the regions where dislocation density and corresponding residual stresses were at their relative maxima (Figs. 7c and 7d). Here the precipitate growth is driven largely by a reduction in strain energy caused by the dislocation-rich microstructure as well as an overall reduction in interfacial energy. The dislocations are essentially driving the thermodynamics of coarsening as is demonstrated by observing the morphology of the globular γ' precipitates which have little, if any, dependence on crystallographic symmetry.

3.3.4. Secondary γ' and Ostwald ripening

Further insight into the rafting behavior following LP and HT is provided by the behavior of secondary γ' (SG) particles dispersed

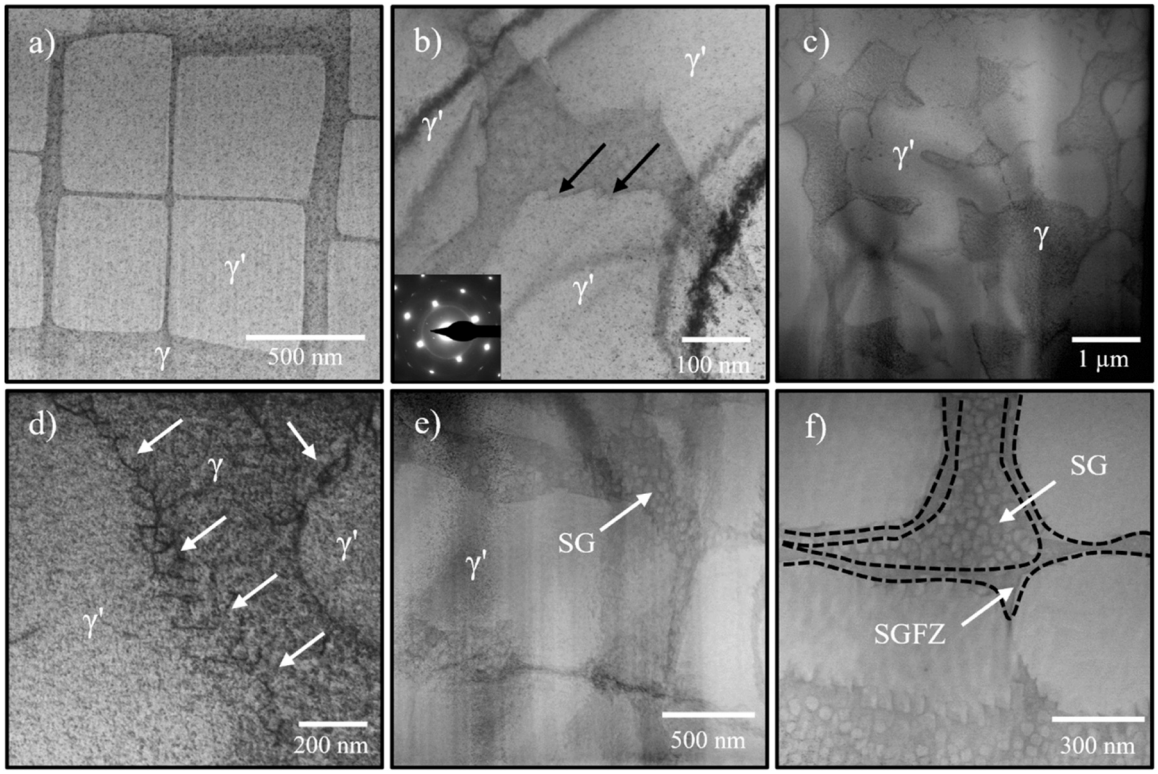

Fig. 7. TEM micrographs showing the (a) untreated microstructure, (b) protrusions along the rafted γ' interface, (c) TPI zone, (d) interfacial dislocations present within the TPI zone, and (e, f) primary and secondary γ' as well as SGFZs following rafting.

throughout the γ phase. In the unpeened specimen (Fig. 7a), SG can be seen in small quantities precipitated between primary γ' without showing any preference for the middle or sides of the γ channel. In the rafted specimens however, there is a distinct zone surrounding the primary γ' precipitates which are completely devoid of secondary phases (herein referred to as the secondary γ' free zone, or SGFZ) (Figs. 7e and 7f). This zone is ~25 nm and affirms that the γ' forming elements that occupied that zone during cooling were drawn into the primary precipitates, causing the interface to move. Moreover, Chen et. al [58] studied the effects of secondary γ' on the rafting behavior of γ' in Ni-based superalloys and showed that the coarsening rate of γ' was largely influenced by their initial size. Larger primary precipitates were seen to grow significantly at the expense of the much smaller secondary γ', which indicates that Ostwald ripening is one of the active mechanisms. In their study they found the limiting state for this behavior to be when the energy required to continue increasing the interfacial area of

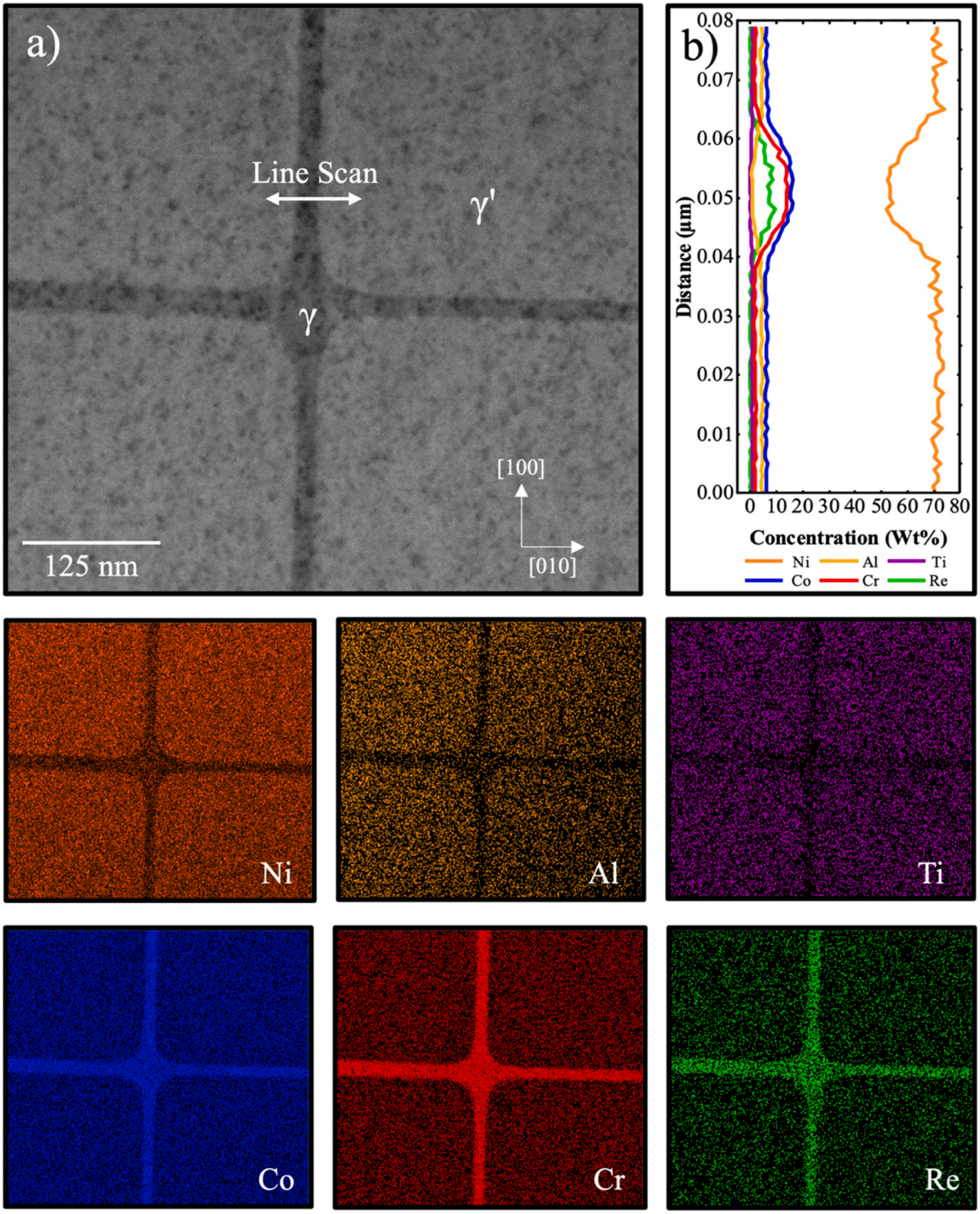

Fig. 8. Untreated specimen: (a) STEM image and (b) EDS line scan, with corresponding element maps listed below.

the precipitates exceeded the thermodynamic driving force for growth which halted coarsening at around 100 nm. The γ' precipitates in the CMSX-4 specimens analyzed in this work before heat treatment had an average side length of ~3–5 μm which is within the range of precipitate sizes observed to be affected by Ostwald ripening [58]. Therefore, it is hypothesized that while the dominant mechanism behind rafting after LP and HT is the mass transport of γ'-forming elements across the vertical γ channels, there is also a contribution from Ostwald ripening of primary γ' at the expense of secondary γ'.

3.3.5. *Interphase solute diffusion during LP-induced rafting*

The final segment of this study lies in the determination of chemical distribution in various manifestations of coarsening. In Fig. 8, a STEM image of the untreated microstructure along with corresponding element maps obtained using energy dispersive x-ray spectroscopy (EDS) of major γ and γ' forming elements are shown (additional EDS

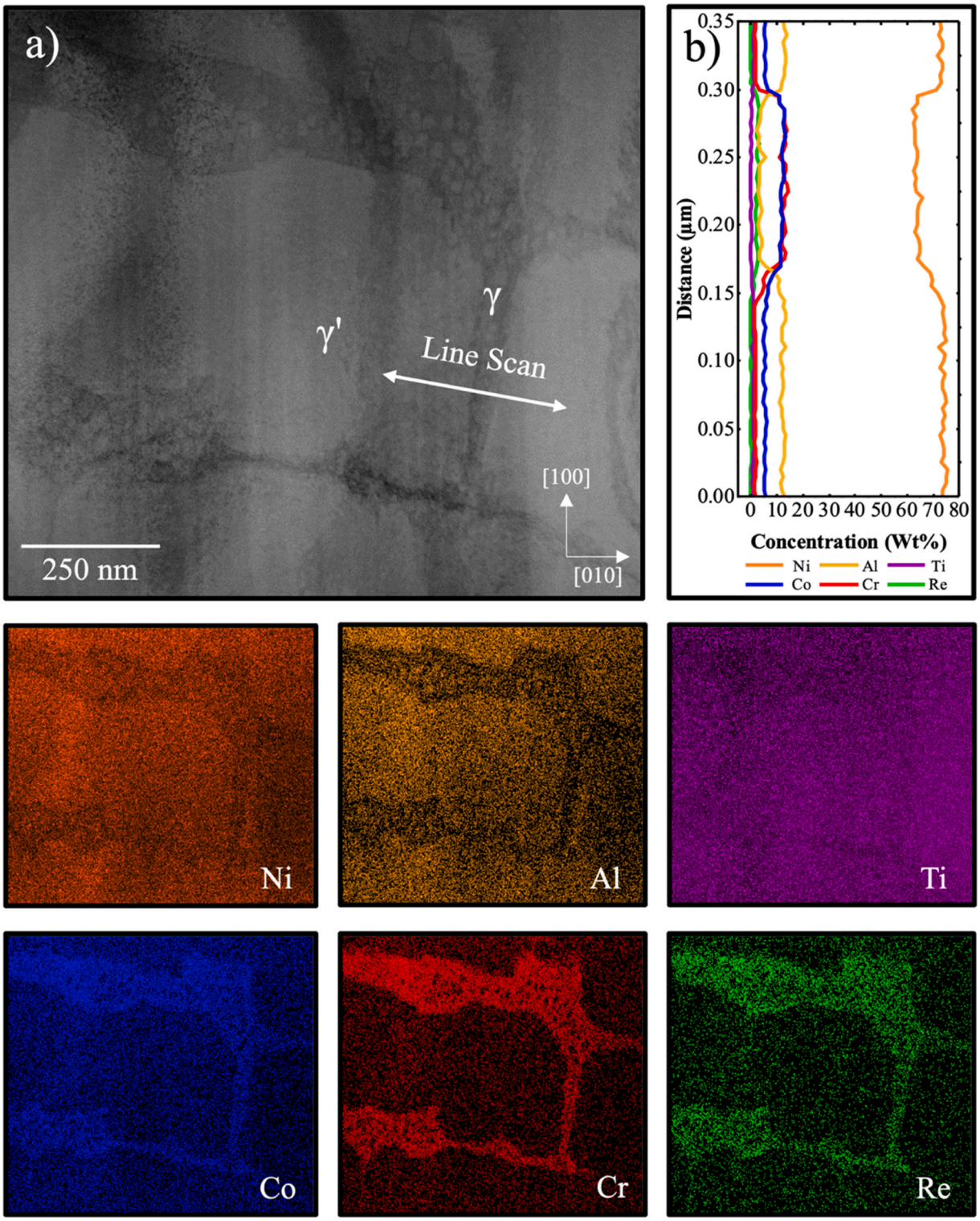

Fig. 9. Heat-treated unpeened specimen: (a) STEM image and (b) EDS line scan, with corresponding element maps listed below.

maps are presented in Figure S.4). It can be observed that the Ni_3Al γ' phase has the highest concentration of its constituent elements as well as Ti, which acts as a substitutional atom on Al sites. Re, Cr, and Co are all dispersed throughout the γ matrix to function as stabilizers within the disordered phase. As such, in the untreated condition, there is very little mixing between the two phases with visibly distinct boundaries.

Following heat treatment, however, the microstructure is noticeably coarsened with a much larger fraction of secondary γ' embedded within the γ channels (Fig. 9a). The precipitation of these secondary phases requires thermodynamically unfavorable diffusion of Al and Ti toward the nucleation sites and Cr, Co, and Re away from them (Fig. 9b) [59]. Additionally, it becomes clear from the EDS results that there is a pronounced depletion of Ni, Al, and Ti, and a relative abundance of Co, Cr, and Re around the primary precipitates, leading to the creation of SGFZs. This is also reflected in the EDS line scan plot in Fig. 9b where the elemental concentration shows significant variability within the γ channel with contributions from the SGFZs and nano-scale secondary precipitates. Lastly, the limited dislocation density within the untreated

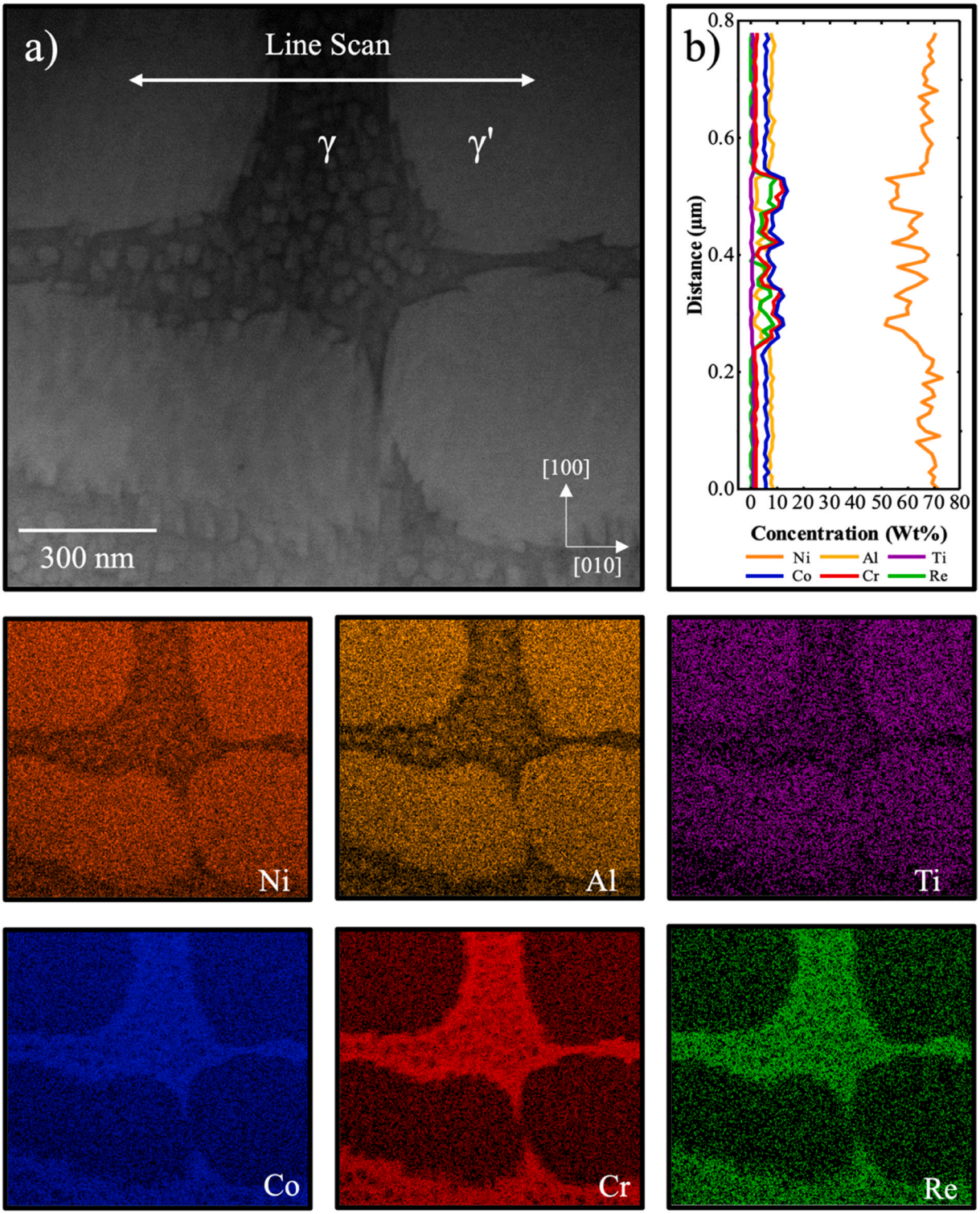

Fig. 10. Rafted specimen: (a) STEM image and (b) EDS line scan, with corresponding element maps listed below.

microstructure denotes that secondary γ' in this case were formed homogeneously within the supersaturated γ channels, likely contributing to their relatively uniform size and spherical geometry.

Similar behavior is observed in the rafted specimen (Fig. 10), though some clear differences are visible due to the high levels of plastic strain this specimen experienced prior to heat treatment. Given that diffusion within the plastically deformed region occurred in the presence of numerous crystalline defects, there is a high likelihood of dislocation-assisted transport of solute atoms as was discussed by [60–62]. Moreover, a recent study by Kontis et al. revealed the presence of solute Cr and Co at dislocations in two different nickel-based superalloys subjected to degradation and creep conditions [52]. The authors observed the segregation of these elements at dislocations within, and at, the interface of the γ' precipitates. They proposed that pipe diffusion of Cr and Co along the dislocations destabilizes the γ matrix and acts as the driving force for the onset of rafting. While the STEM-EDS results here do not definitively show the solute element partitioning consistent with Kontis et al., this is likely resulting from the spatial resolution

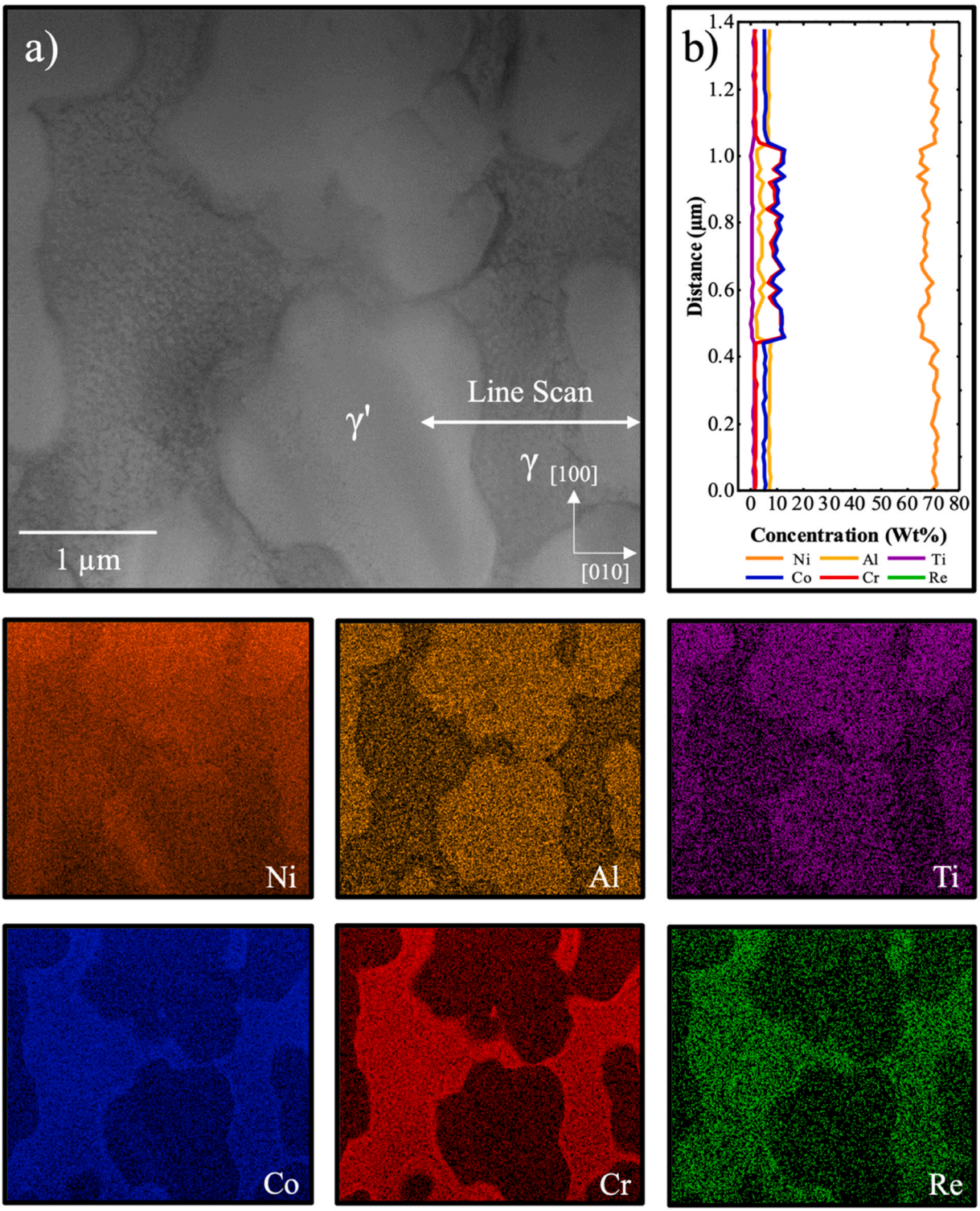

Fig. 11. TPI zone: (a) STEM image and (b) EDS line scan, with corresponding element maps listed below.

challenges of STEM-EDS in comparison to the atom probe tomography methods that were used in their work. Moreover, the solute partitioning of Cr and Co to the interphase interface in our results lends viability to the pipe diffusion model. Differing further from the heat-treated unpeened specimen, the dislocation nodes within the γ matrix of the rafted specimen acted as heterogeneous nucleation sites [60] by reducing the barrier for secondary precipitate nucleation. In stark contrast to the other specimens, the TPI specimen (Fig. 11) shows bloated γ' phases rich in Ni, Al, and Ti with few, if any, secondary precipitates. In this case, the dislocation-rich microstructure enabled rapid diffusion of γ' formers into the primary precipitates and enabled their growth.

4. Conclusions

In this work, the effects of severe plastic deformation imparted by LP on the directional coarsening behavior of a single crystal Ni-based superalloy following high-temperature exposure were investigated. It was revealed that LP can influence the directional coarsening behavior of γ' precipitates depending on the magnitude and depth of residual stresses, as well as the density of dislocations generated by LP. Lastly, the mechanisms that govern the rafting thermodynamics, such as dislocation-aided interface growth, solute diffusion, and stress superposition were uncovered. The main findings from this work are:

- LP generated a surface layer with compressive stresses ranging from -400 MPa to -800 MPa and transitioned to a state of tensile stress on the order of 200 MPa at greater depths. These contrasting stress states led to horizontal and vertical rafting up to a depth of 1 mm before returning to a state of non-directionally coarsened material at depths greater than 5 mm. The top surface of the LPed material experienced the greatest level of deformation and consequently, coarsening was largely driven by an overall reduction in plastic strain energy, resulting in misshapen, globular γ' phases.
- Plastic strain near the LPed surface was measurably increased with lattice misorientation values around 5°. Following heat treatment, plastic strain completely relaxed due to rafting-aided recovery and defect reorganization. No RX was observed.
- Secondary γ' precipitates were observed occupying the γ channels between rafted precipitates, showing the diffusion and subsequent supersaturation of solute elements Al and Ti in the matrix phase. Additionally, precipitate free zones surrounding the primary rafted precipitates were found to be a result of solute depletion following coarsening.
- Plastic deformation from LP altered the coarsening behavior of the γ' phase into the surrounding matrix by creating interfacial dislocations that destabilized the misfit strain and reduced the energy barrier for coarsening.

Understanding the effect that surface hardening processes have on the rafting behavior of single crystalline Ni-based superalloys is crucial for the continual improvement of this robust class of materials. The possibilities of localized surface strengthening for enhancing the defensive capabilities of turbine blades or other engine components against surface-initiated damage mechanisms are very promising. In the engineering of these processes though, one must determine how the residual stress state and defect environment affect the microstructural response to thermal input.

Appendix

Funding

The project was supported by the National Science Foundation, CMMI, and the Advanced Manufacturing Program (Award Number: 2029059).

CRediT authorship contribution statement

Noah Holtham: Writing – review & editing, Writing – original draft, Validation, Methodology, Investigation, Formal analysis, Data curation, Conceptualization. **Nicholas Brooks:** Writing – review & editing, Methodology, Investigation. **Russell Rowe:** Writing – review & editing, Methodology, Investigation. **Lloyd Hackel:** Writing – review & editing, Validation, Investigation. **Alireza Zargaran:** Writing – review & editing, Investigation. **Keivan Davami:** Writing – review & editing, Validation, Supervision, Funding acquisition, Conceptualization.

Declaration of Competing Interest

The authors declare that they have no known competing financial interests or personal relationships that could have appeared to influence the work reported in this paper.

Data availability

Data will be made available on request.

Acknowledgments

The authors would like to acknowledge The University of Alabama's Core Analytical Facility (CAF) for the use of facilities as well as Curtiss-Wright Metal Surface Technologies for conducting the laser peening treatments for this work. The authors would additionally like to thank the Alabama Water Institute and Alabama Transportation Institute. The authors gratefully acknowledge DURIP funding from the Air Force Office of Scientific Research (AFOSR).

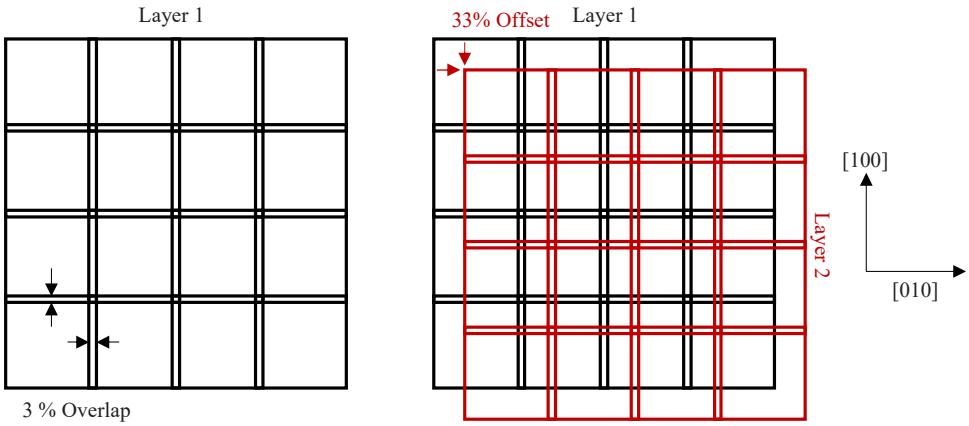

Fig A.1. . Schematic of the LP procedure showing overlap and offset geometry.

Appendix A. Supporting information

Supplementary data associated with this article can be found in the online version at doi:10.1016/j.jallcom.2024.175851.

References

[1] W. Cai, W.D. Nix, Imperfections in Crystalline Solids, Cambridge University Press, Cambridge, 2016.
[2] J. Coakley, D. Ma, M. Frost, D. Dye, D.N. Seidman, D.C. Dunand, H.J. Stone, Lattice strain evolution and load partitioning during creep of a Ni-based superalloy single crystal with rafted γ′ microstructure, Acta Mater. 135 (2017) 77–87.
[3] S. Huang, K. An, Y. Gao, A. Suzuki, Determination of γ/γ′ lattice misfit in Ni-based single-crystal superalloys at high temperatures by neutron diffraction, Metall. Mater. Trans. A 49 (3) (2018) 740–751.
[4] N. Matan, D.C. Cox, C.M.F. Rae, R.C. Reed, On the kinetics of rafting in CMSX-4 superalloy single crystals, Acta Mater. 47 (7) (1999) 2031–2045.
[5] F.R.N. Nabarro, Rafting in superalloys, Metall. Mater. Trans. A 27 (1996) 513–530.
[6] M. Ott, H. Mughrabi, Dependence of the high-temperature low-cycle fatigue behaviour of the monocrystalline nickel-base superalloys CMSX-4 and CMSX-6 on the γ/γ'-morphology, Mater. Sci. Eng. A Struct. Mater.: Prop., Microstruct. Process. 272 (1) (1999) 24–30.
[7] M. Kamaraj, Rafting in single crystal nickel-base superalloys — An overview, Sadhana 28 (1) (2003) 115–128.
[8] A. Goodfellow, Strengthening mechanisms in polycrystalline nickel-based superalloys, Mater. Sci. Technol. 34 (15) (2018) 1793–1808.
[9] Z. Tang, K. Wang, Y. Geng, X. Dong, W. Duan, X. Sun, X. Mei, An investigation of the effect of warm laser shock peening on the surface modifications of [001]-oriented DD6 superalloy, Int. J. Adv. Manuf. Technol. 113 (7-8) (2021) 1973–1988.
[10] H. Biermann, U. Tetzlaff, B. von Grossmann, H. Mughrabi, V. Schulze, Rafting in monocrystalline nickel-base superalloys induced by shot peening, Scr. Mater. - Scr. Mater. 43 (2000) 807–812.
[11] I. Bogachev, K.M. Knowles, G.J. Gibson, High temperature behaviour of a mechanically surface hardened single crystal nickel-based superalloy, Materialia 23 (2022) 101438.
[12] X. Yang, S. Li, H. Qi, Effect of high-temperature hot corrosion on the low cycle fatigue behavior of a directionally solidified nickel-base superalloy, Int. J. Fatigue 70 (2015) 106–113.
[13] A.S. Gill, A study of the effects of laser shock peening on residual stress, microstructure and local properties of IN718 nickel-base superalloy, university of cincinnati, Ann. Arbor. MI USA (2012) 341.
[14] N. Holtham, K. Davami, Laser surface treatment of Inconel 617 for next-generation nuclear reactors: a strengthening mechanisms study, Mater. Charact. 202 (2023) 113024.
[15] N. Brooks, M. Vaseghi, L. Hackel, K. Davami, Microstructural and mechanical characterization of pearlitic steel after high intensity laser peening and shot peening, Manuf. Lett. 38 (2023) 35–39.
[16] K.S. Chin, S. Idapalapati, D.T. Ardi, Thermal stress relaxation in shot peened and laser peened nickel-based superalloy, J. Mater. Sci. Technol. 59 (2020) 100–106.
[17] Single-crystal superalloys for blade applications, in: R.C. Reed (Ed.), The Superalloys: Fundamentals and Applications, Cambridge University Press, Cambridge, 2006, pp. 121-216.
[18] J.H. Miller, Lloyd; Dane, Clifford; Zapata, Luis, High Power Regenerative Laser Amplification, in: U.S.P. Office (Ed.) United States, 1994.
[19] P. Peyre, R. Fabbro, P. Merrien, H.P. Lieurade, Laser shock processing of aluminium alloys. Application to high cycle fatigue behaviour, Mater. Sci. Eng.: A 210 (1) (1996) 102–113.
[20] D. Devaux, R. Fabbro, L. Tollier, E. Bartnicki, Generation of shock waves by laser-induced plasma in confined geometry, J. Appl. Phys. 74 (4) (1993) 2268–2273.
[21] S. Nath, P. Shukla, X. Shen, J. Lawrence, A. Behera, Estimation of laser shock peening induced plastic deformation in Hastelloy-X superalloys, Int. J. Peen. Sci. Technol. 3 (2019) 233–257.
[22] Y. Sun, Z. Hou, Z. Yao, Y. Hu, Gradient structure and mechanical behavior induced by multiple laser peening in 304 austenitic stainless steel, Int. J. Adv. Manuf. Technol. 120 (5) (2022) 3383–3392.
[23] H. Chen, A. Feng, J. Li, T. Jia, Y. Liu, Effects of multiple laser peening impacts on mechanical properties and microstructure evolution of 40CrNiMo Steel, J. Mater. Eng. Perform. 28 (5) (2019) 2522–2529.
[24] C.B. Dane, L. Hackel, J. Daly, J. Harrisson, Laser peening of metals- enabling laser technology, MRS Proc. 499 (1997) 73.
[25] Y. Geng, X. Dong, K. Wang, X. Mei, Z. Tang, W. Duan, Evolutions of microstructure, phase, microhardness, and residual stress of multiple laser shock peened Ni-based single crystal superalloy after short-term thermal exposure, Opt. Laser Technol. (123) (2020).
[26] Y. Geng, Y. Mo, H. Zheng, G. Li, K. Wang, Effect of laser shock peening on the hot corrosion behavior of Ni-based single-crystal superalloy at 750°C, Corros. Sci. 185 (2021) 109419.
[27] B. Rakoczy, M. Rutkowski, R. Grudzień-Rakoczy, W. Cygan, A. Ratuszek, Zielińska-Lipiec, Analysis of γ′ precipitates, carbides and nano-borides in heat-treated Ni-based superalloy using SEM, STEM-EDX, and HRSTEM, Materials 13 (19) (2020) 4452.
[28] B.D. Cullity, Elements of X-RAY DIFFRACTION, Second ed., Addison-Wesley Publishing Company, Inc.1978.
[29] A. Umapathi, S. Swaroop, Measurement of residual stresses in titanium alloys using synchrotron radiation, Measurement 140 (2019) 518–525.
[30] S. Keller, S. Chupakhin, P. Staron, E. Maawad, N. Kashaev, B. Klusemann, Experimental and numerical investigation of residual stresses in laser shock peened AA2198, J. Mater. Process. Technol. 255 (2018) 294–307.
[31] M. Kattoura, S.R. Mannava, D. Qian, V.K. Vasudevan, Effect of laser shock peening on residual stress, microstructure and fatigue behavior of ATI 718Plus alloy, Int. J. Fatigue 102 (2017) 121–134.
[32] D. Siebörger, H. Knake, U. Glatzel, Temperature dependence of the elastic moduli of the nickel-base superalloy CMSX-4 and its isolated phases, Mater. Sci. Eng.: A 298 (1) (2001) 26–33.
[33] ASTM, Standard Test Method for Microindentation Hardness of Materials, 2021, p. 5.
[34] J.V. Goerler, I. Lopez-Galilea, L. Mujica Roncery, O. Shchyglo, W. Theisen, I. Steinbach, Topological phase inversion after long-term thermal exposure of nickel-base superalloys: experiment and phase-field simulation, Acta Mater. 124 (2017) 151–158.
[35] T. Pollock, A. Argon, Directional coarsening in nickel-base single crystals with high volume fractions of coherent precipitates, Acta Metall. Et. Mater. 42 (6) (1994) 1859–1874.
[36] N. Holtham, K. Davami, A review of laser peening methods for single crystal Ni-based superalloys, Metals (2022).
[37] M. Munther, T. Martin, A. Tajyar, L. Hackel, A. Beheshti, K. Davami, Laser shock peening and its effects on microstructure and properties of additively manufactured metal alloys: a review, Eng. Res. Express 2 (2) (2020) 022001.
[38] J. Zhang, L. Liu, T. Huang, J. Chen, K. Cao, X. Liu, J. Zhang, H. Fu, Coarsening kinetics of γ′ precipitates in a Re-containing Ni-based single crystal superalloy during long-term aging, J. Mater. Sci. Technol. 62 (2021) 1–10.

[39] R.C. Reed, D.C. Cox, C.M.F. Rae, Kinetics of rafting in a single crystal superalloy: effects of residual microsegregation, Mater. Sci. Technol. 23 (8) (2007) 893–902.
[40] P. Pagliaro, M.B. Prime, H. Swenson, B. Zuccarello, Measuring multiple residual-stress components using the contour method and multiple cuts, Exp. Mech. 50 (2) (2010) 187–194.
[41] F. Hosseinzadeh, J. Kowal, P.J. Bouchard, Towards good practice guidelines for the contour method of residual stress measurement, J. Eng. 2014 (8) (2014) 453–468.
[42] H.K. Amarchinta, R.V. Grandhi, A.H. Clauer, K. Langer, D.S. Stargel, Simulation of residual stress induced by a laser peening process through inverse optimization of material models, J. Mater. Process. Technol. 210 (14) (2010) 1997–2006.
[43] Z. Zhou, A.S. Gill, D. Qian, S.R. Mannava, K. Langer, Y. Wen, V.K. Vasudevan, A finite element study of thermal relaxation of residual stress in laser shock peened IN718 superalloy, Int. J. Impact Eng. 38 (7) (2011) 590–596.
[44] D.A. Porter, K.E. Easterling, M.Y. Sherif, Phase Transformations in Metals and Alloys, CRC Press2021.
[45] A. Morançais, M. Fèvre, M. François, N. Guel, S. Kruch, P. Kanouté, A. Longuet, Residual stress determination in a shot-peened nickel-based single-crystal superalloy using X-ray diffraction, J. Appl. Crystallogr. 48 (6) (2015) 1761–1776.
[46] I. Bogachev, K.M. Knowles, G.J. Gibson, Electron backscattered diffraction analysis of cold work in a shot peened single crystal nickel superalloy, Materialia 14 (2020).
[47] I. Bogachev, K.M. Knowles, G.J. Gibson, Deep cold rolling of single crystal nickel-based superalloy CMSX-4, Materialia 20 (2021) 101240.
[48] L. Hackel, J.R. Rankin, A. Rubenchik, W.E. King, M. Matthews, Laser peening: A tool for additive manufacturing post-processing, Additive Manufacturing 24 (2018) 67-75.
[49] T. Link, A. Epishin, M. Paulisch, T. May, Topography of semicoherent γ/γ'-interfaces in superalloys: investigation of the formation mechanism, Mater. Sci. Eng.: A 528 (19) (2011) 6225–6234.
[50] H. Long, Y. Liu, D. Kong, H. Wei, Y. Chen, S. Mao, Shearing mechanisms of stacking fault and anti-phase-boundary forming dislocation pairs in the γ' phase in Ni-based single crystal superalloy, J. Alloy. Compd. 724 (2017) 287–295.
[51] R.A. Rowe, N. Holtham, P. Allison, A. Palazotto, K. Davami, A comparison of high strain rate response and adiabatic shear band formation in additively and traditionally manufactured Inconel 718, Mater. Charact. 207 (2024) 113506.
[52] P. Kontis, Z. Li, D.M. Collins, J. Cormier, D. Raabe, B. Gault, The effect of chromium and cobalt segregation at dislocations on nickel-based superalloys, Scr. Mater. 145 (2018) 76–80.
[53] L.J. Carroll, Q. Feng, T.M. Pollock, Interfacial dislocation networks and creep in directional coarsened Ru-containing nickel-base single-crystal superalloys, Metall. Mater. Trans. A 39 (6) (2008) 1290–1307.
[54] T.M. Pollock, A.S. Argon, Directional coarsening in nickel-base single crystals with high volume fractions of coherent precipitates, Acta Metall. Et. Mater. 42 (6) (1994) 1859–1874.
[55] R.A. MacKay, L.J. Ebert, The development of directional coarsening of the γ' precipitate in superalloy single crystals, Scr. Metall. 17 (10) (1983) 1217–1222.
[56] T.P. Gabb, S.L. Draper, D.R. Hull, R.A. Mackay, M.V. Nathal, The role of interfacial dislocation networks in high temperature creep of superalloys, Mater. Sci. Eng.: A 118 (1989) 59–69.
[57] R. Wu, S. Sandfeld, A dislocation dynamics-assisted phase field model for Nickel-based superalloys: the role of initial dislocation density and external stress during creep, J. Alloy. Compd. 703 (2017) 389–395.
[58] W. Chen, J.P. Immarigeon, Thickening behaviour of γ' precipitates in nickel base superalloys during rafting, Scr. Mater. 39 (2) (1998) 167–174.
[59] S. Hayashi, W. Wang, D.J. Sordelet, B. Gleeson, Interdiffusion behavior of Pt-modified γ-Ni+ γ'-Ni 3 Al alloys coupled to Ni-Al-based alloys, Metall. Mater. Trans. A 36 (2005) 1769–1775.
[60] S. Xiang, S. Mao, H. Wei, Y. Liu, J. Zhang, Z. Shen, H. Long, H. Zhang, X. Wang, Z. Zhang, X. Han, Selective evolution of secondary γ' precipitation in a Ni-based single crystal superalloy both in the γ matrix and at the dislocation nodes, Acta Mater. 116 (2016) 343–353.
[61] M. Legros, G. Dehm, E. Arzt, T.J. Balk, Observation of giant diffusivity along dislocation cores, Science 319 (5870) (2008) 1646–1649.
[62] B. Dutta, E.J. Palmiere, C.M. Sellars, Modelling the kinetics of strain induced precipitation in Nb microalloyed steels, Acta Mater. 49 (5) (2001) 785–794.